III.D.4. 2D and 1D Digital Fourier Reconstruction Methods

Images of biological specimens can be processed in a variety of different ways, some of which are more popular or better established than others. Most processing methods are relatively straight-forward, but occasionally one will encounter a difficult specimen that may require the use of a novel strategy. In general, the type of specimen examined dictates the type of method applied. A convenient classification of specimens can be made according to the shape or symmetry of the specimen.

Though ultimately our interest is in learning the full three-dimensional structure of the molecules that we image in the microscope, it can be quite informative to compute image recon-structions by Fourier methods in two dimensions, or sometimes even in one dimension (*e.g.* helices). Also, a large number of biological macromolecules such as membranes, cell walls, and some naturally occurring crystals are planar (2D) objects and make excellent subjects for Fourier image analysis in both 2D and 3D.

a. 2D Fourier averaging of specimens with 2D translational symmetry

Planar objects are considered two-dimensional because one dimension is smaller or much smaller than the other two. For many specimens that fit this description, the shortest dimension is often 50 nm or smaller and includes only one or a few 'unit cells' in the direction normal to the plane of the specimen (parallel to the electron beam when the specimen is untilted in the electron microscope). Though these type specimens can be analyzed with optical or photographic superposition methods, the digital Fourier methods are particularly powerful because they are quantitative and rigorous.

The methods and applications of 2D Fourier image processing for analyzing images of planar specimens can be found in numerous primary literature articles (see Reference Reading List, pp.6-7, for several examples). Examples of planar specimens that have been studied by 2D and 3D reconstruction techniques are the purple membrane, cytochrome oxidase vesicles, membrane-bound ribosomes, actin filament bundles and actin sheets, tubulin sheets, bacterial cell layers, RNA polymerase crystals, gap junction membranes, and tropomyosin crystals to name a few.

The following list briefly outlines the basic steps involved in analyzing the images of regular (*i.e.* highly ordered or crystalline) planar specimens. After the basic strategy is outlined, several figures are included to help illustrate various aspects of the procedures.

Protocol for Fourier averaging images of 2D crystals:

1) After a visual screening step (to toss obvious bad micrographs), select a subset of micrographs that give the highest quality optical diffraction patterns. Highly coherent crystalline areas give strong, sharp Bragg reflections to 'high' resolution (*e.g.* ~15-20Å for negatively stained crystals recorded with minimum irradiation techniques). Look for minimal radiation damage, astigmatism, and specimen drift or vibration and for 'best' defocus (*i.e.* giving the desired CTF characteristics) and highest resolution (most spots in all directions).

2) Digitize the micrograph at a sampling interval fine enough *not* to limit image resolution but not too fine or the digitized image will consist of many more pixels than is necessary, which results in needless computations.

3) Box (window) out the desired region of interest, making sure to exclude, if possible, as much of the unneeded portions of the digitized image as is practical. This is easy to do with 'perfect' specimens like catalase crystals that grow large enough (several μm^2) to fill the entire field of view at 30,000 magnification or higher.

4) Float the boxed image by subtracting from every pixel within the image the average value of the pixels that form the **perimeter** of the box.

5) Fourier transform the boxed, digitized image. With some software, the image must first be padded with zeroes so the image that is transformed has dimensions that are a power of two

such as 256^2 or 512^2 or 256 x 512 or 128 x 1024, etc. Generally, owing to Friedel's Law, just the 'top half' of the Fourier transform need be computed (*i.e.* k values 0 or positive only). The transform is stored as structure factor A (real) and B (imaginary) parts. Hence, for a 512^2 image, the resulting transform will consist of 512 by 256 complex numbers.

6) Display and index the diffraction pattern on a graphics workstation. This indexing could be performed on an optical diffraction pattern, however, the digital transform allows one to quantitatively check other properties of the specimen such as the presence of certain plane group symmetries. The existence, for example, of a three-fold axis of symmetry at the unit cell origin, for noise free data, will restrict the structure factor phases to be multiples of 120°. The noisier the image the more the symmetry related structure factor phases will deviate from the 120° relationship.

7) Perform either pseudo-optical filtering or Fourier averaging of the data. In pseudo-optical filtering, filter masks can be computer generated with 'holes' of a specified size distributed on a lattice either covering the whole transform or limited at some specified upper resolution boundary. The computer-generated mask is then multiplied times the Fourier transform and the result is back-transformed to generate the filtered image. A number of variations of pseudo-optical filtering can be employed. For example, low and/or high-pass as well as lattice filter masks can be generated to perform different types of filtering of the data. Also, the holes can be given a Gaussian weight so the value at the center of the hole is 1.0 but then drops to 1/exp at the edge of the hole where the mask has a value of zero. The Fourier filtered image is obtained by back transforming the masked transform.

To compute a Fourier-averaged reconstruction, in which **all** unit cells within the boxed area are averaged together, the data in the vicinity of each Bragg reflection are averaged or integrated together or are sampled to reduce the data to a single structure factor. This is equivalent to the pseudo-filtering experiment in which the hole size is reduced to zero radius, which has the effect of convoluting the image with a lattice that includes every unit cell contained within the boxed region of the micrograph. This convolution forces the image to obey a perfect translational symmetry (*i.e.* p1 plane group). Again, a number of variations of this process can be implemented to produce different Fourier averages. The average structure of a single unit cell (all unit cells are identical in a Fourier average) is obtained by back transforming the structure factors (Fourier synthesis).

8. Assess and apply additional symmetry if evidence exists that the specimen obeys symmetry higher than p1. This must be performed with due caution because it is very easy to apply *any* symmetry you want with computer programs. Hence, when you impose additional symmetry, the specimen will, of course, exhibit whatever symmetry has been applied.
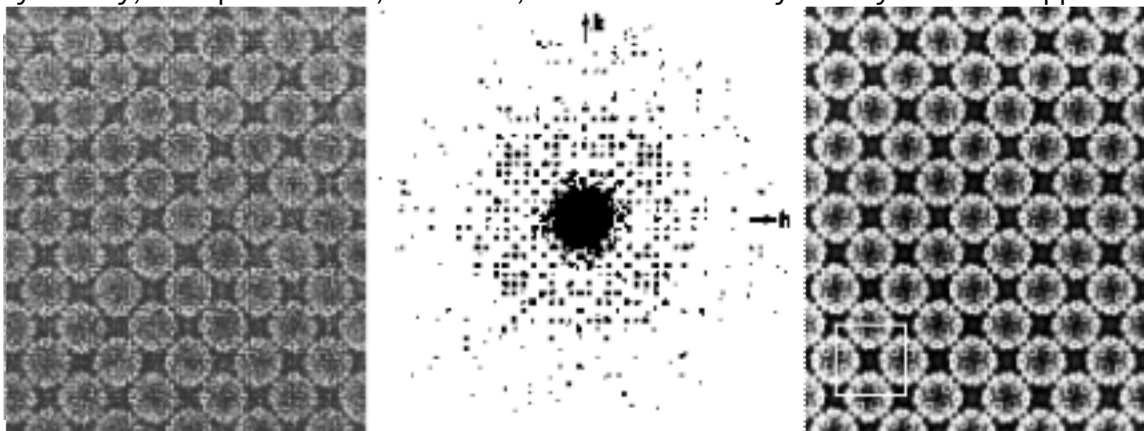

Fig.III.90. Fourier averaging of a negatively stained crystal of cowpea chlorotic mottle virus (CCMV). (Left) Small portion of CCMV 2D crystal. (Center) Optical diffraction pattern of small region of CCMV crystal exhibits pseudo tetragonal symmetry (p4) with a=b=375Å. The true unit cell is $p2_12_1$ as exhibited by the phase relationships in the Bragg reflections (see Fig.III.91). (Right) Grey level display of the Fourier averaged image of the CCMV crystal, with $p2_12_1$ symmetry imposed. The unit cell (white box) contains two virus particles, related to each other by a rotation of ~86°.
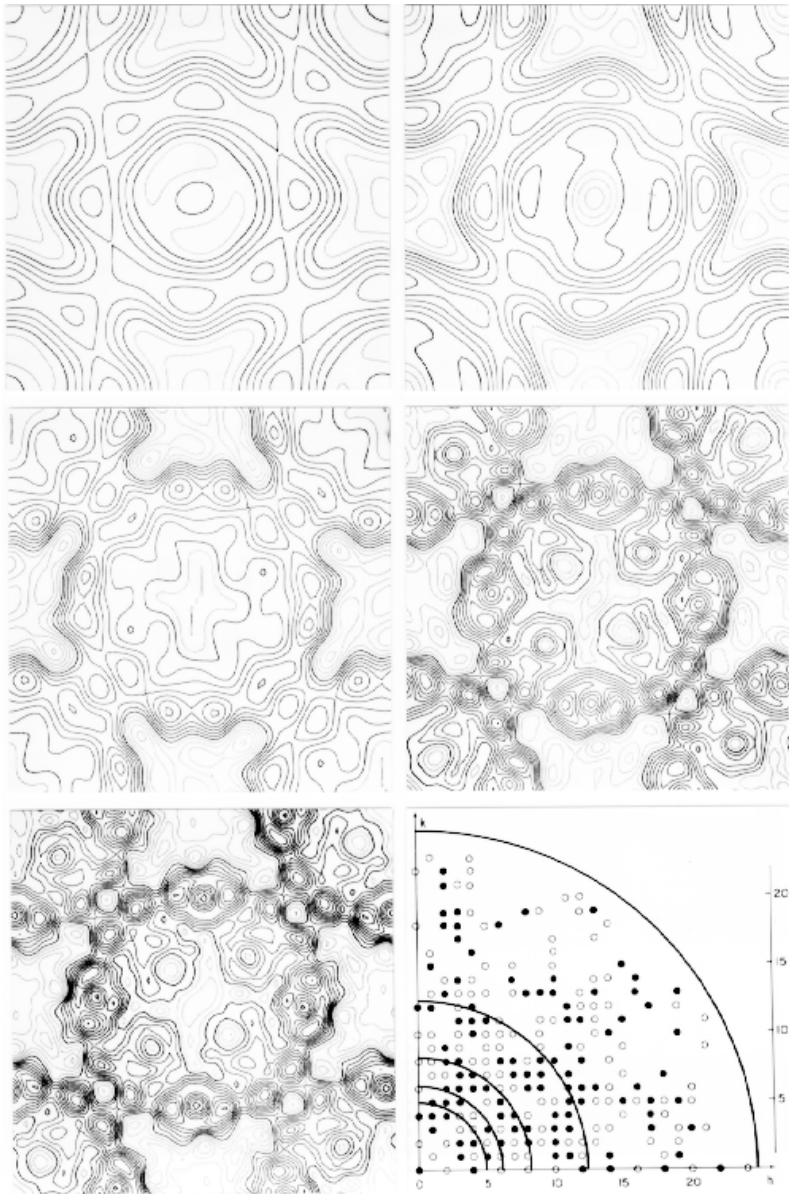
Fig.III.91. CCMV Fourier average at increasing resolution limits. Five contoured views of a single CCMV particle from the Fourier average shown in Fig.III.90, are displayed at progressively higher resolutions, from 75Å (top left) to 60 (top right) to 45 and 30Å (middle panels) to 15Å (bottom left). In each contour display, the darker lines outline the stain excluding regions and the lighter lines outline the negative stain. (Bottom right) A representation of one quarter of the CCMV transform, with large circles indicting the resolution limits imposed to produce the displays in the other panels and open and closed small circles indicate the phases (0 or 180°, respectively) of each of the observed Bragg reflections. The phases obey the relationships required by plane group $p2_12_1$. Also, note the systematic absences along the h and k directions of the diffraction pattern.
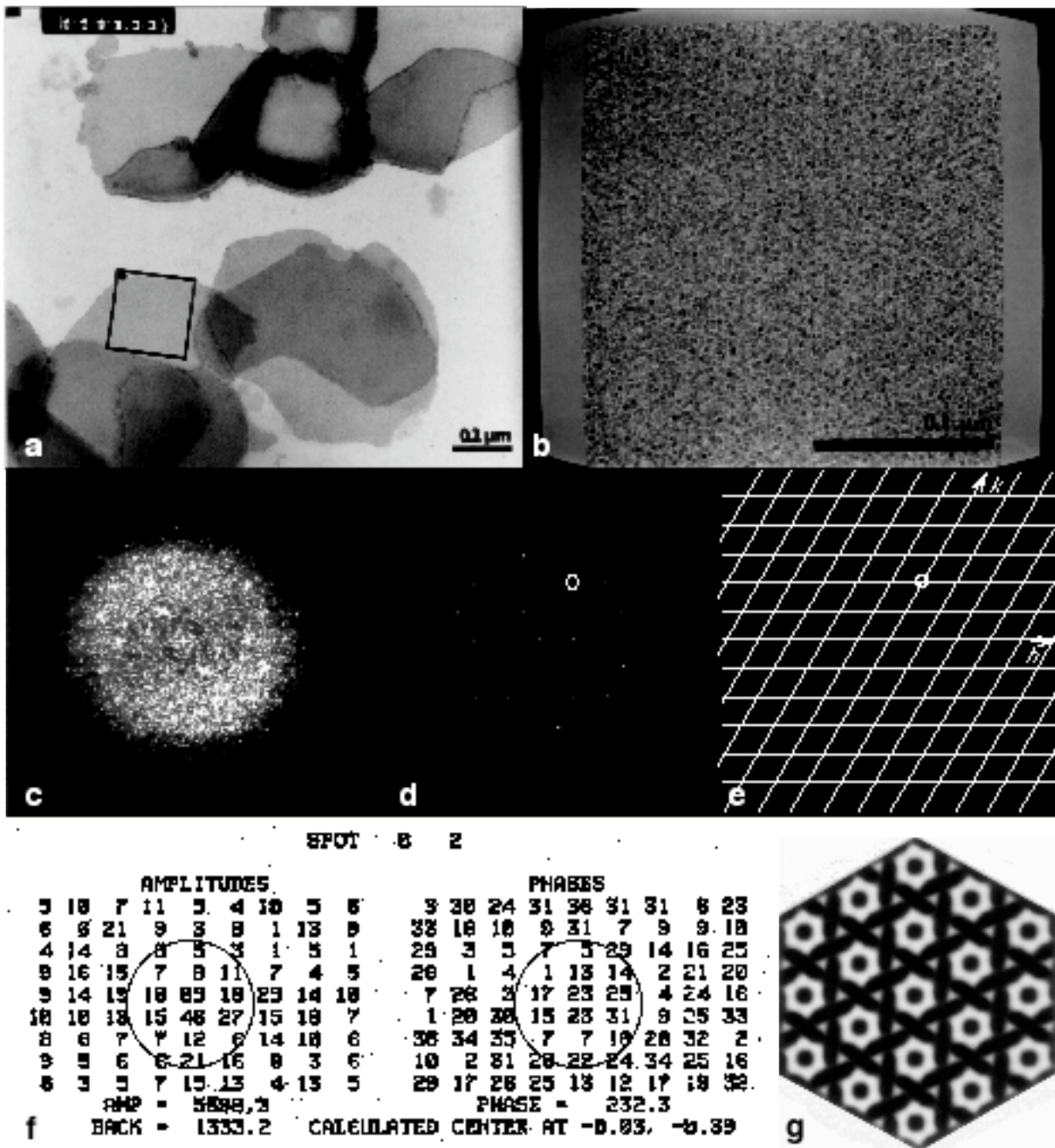
Fig.III.92. Fourier averaging of image of negatively stained gap junction membrane. (a) Low magnification view of entire micrograph shows several stained gap junction membranes. The area outlined with the square black box was digitized and displayed on a raster graphics device. In some regions, two or three junction membranes lie stacked above one another on the EM grid. (b) Display of region boxed and floated from the original micrograph shown in (a). (c) Computer graphics display of the intensities in the Fourier transform of (b), with the transform scaled to reveal the contrast transfer function of the microscope. Note the slight astigmatism revealed in the non-circular noise pattern. (d) Same as (c) but scaled to show just the most intense peaks in the transform. The $h,k=0,2$ Bragg reflection is encircled. (e) Same as (d) with a reciprocal lattice overlay. (f) Structure factor amplitudes (on left) and phases (on right) extracted from the 512^2 transform for the region centered about the $h,k=0,2$ reflection circled in (d,e). Each phase value is divided by 10 (e.g. a phase of 23 at the center actually represents a phase of 230°). A single structure factor amplitude (5598.3) is integrated from within a circle like the one depicted, centered at position -0.03 in x and -0.39 in y, with respect to the grid point in the center of each window of data points (amp=85, phase=23). The single structure factor phase (232.3°) is calculated by interpolation from the four data points closest to the calculated center of the 0,2 spot. (g) Fourier average computed by back transformation of the set of structure factors extracted as shown in (f).
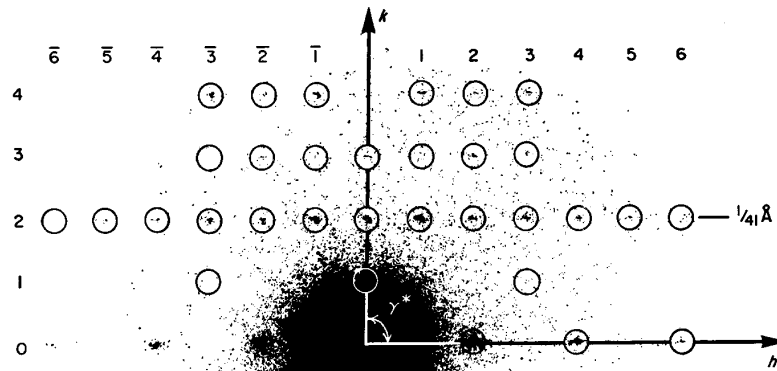
Fig.III.93. Indexed, optical diffraction pattern of tubulin Zn sheets which were negatively stained with uranyl acetate. This image was recorded under minimal dose conditions (~20e⁻/Å²). The equatorial and meridional axes are labeled h and k, respectively. The intensity distribution obeys a near perfect mm relationship (i.e. each spot has two mirror-related mates reflected across the h and k mirror lines. Measurement of the a* and b* dimensions in the orthogonal reciprocal lattice indicates an orthogonal (rectangular) unit cell with a=97Å, b=82Å, and γ=90°. Systematic absences along the h direction reveal the presence of a 2_1 screw axis parallel to the a cell direction. (From Baker and Amos, 1978, p.96)
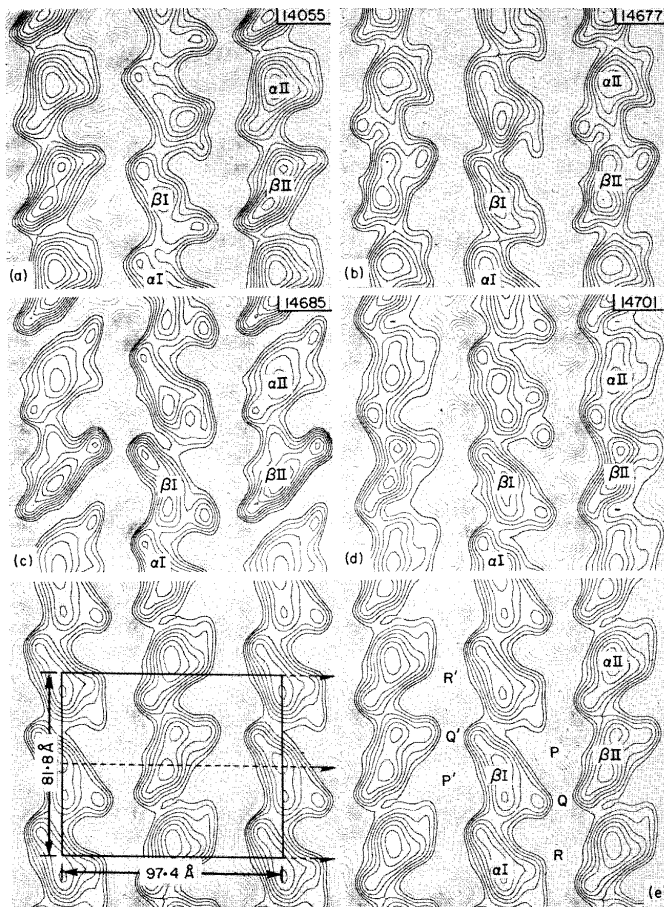

Fig.III.94. Image reconstructions of four individual Zn tubulin sheets and their average (bottom panel). Dark lines represent contours of density form zero to successively higher positive amplitudes. Light lines represent contours at negative amplitudes. (a-d) Individual reconstructions from four images, showing corresponding regions of the structure. Subunits are labeled to indicate possible pairing of monomers into heterodimers, and to show the relationship of dimers in adjacent protofilaments. The α and β labels are arbitrary. (e) Average reconstruction of the four sheets (a) to (d), showing contents of several unit cells. One cell is outlined, and the positions of the dyad screw axes are indicated by broken lines with half arrows. Note, however, that NONE of these reconstructions have had a perfect screw axis symmetry enforced. (From Baker and Amos, 1978, p.99)
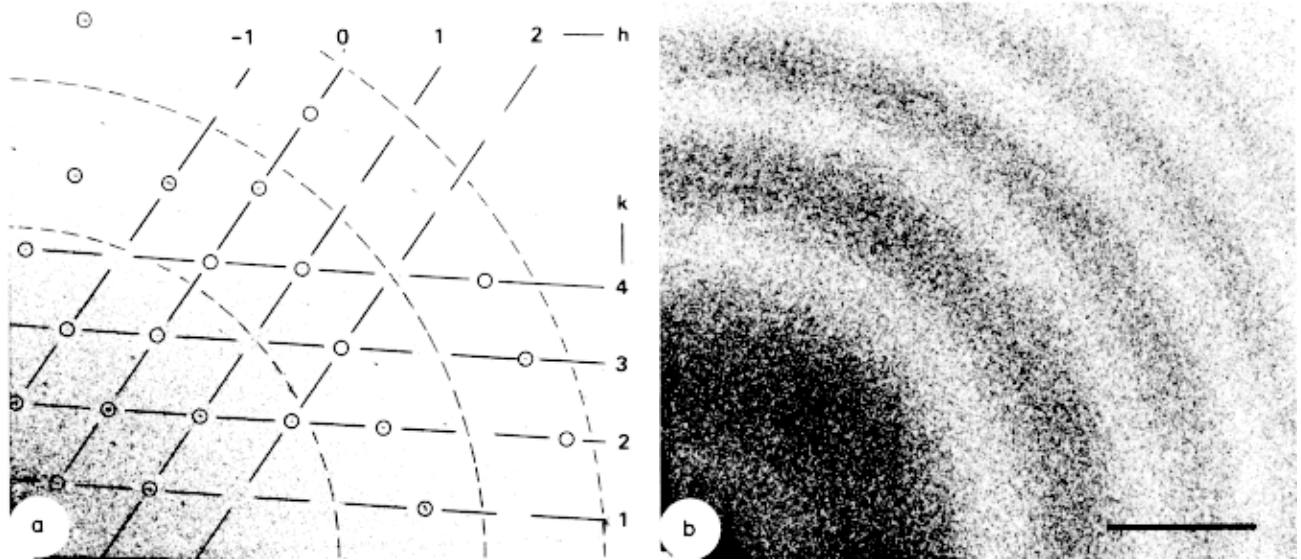
Fig.III.95. Optical transform quadrants of unstained purple membrane micrographs taken in bright-field microscopy: (a) Low dose image, (b) High dose image. Diffraction bar = 1/33Å. (From Misell, p.174; adapted from Unwin and Henderson, 1975)
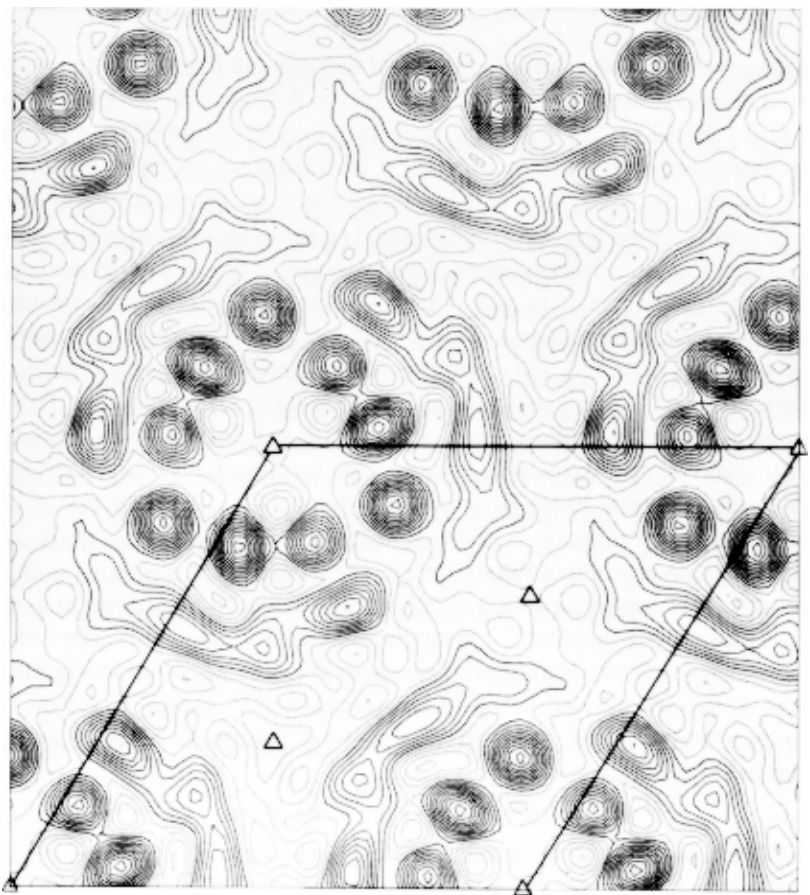

Fig.III.96. Contour map of the projected structure of purple membrane at 7Å resolution. Thicker lines show positive contours; positive peaks are due to high concentrations of scattering material (protein). Low density regions indicated by thinner lines are due to lipid and glucose. Unit cell dimensions are 62Å x 62Å. (From Misell, p.175; adapted from Unwin and Henderson, 1975)

b. 2D averaging of objects with point group symmetry: rotational filtering

Specimens that only possess rotational symmetry, such as individual oligomeric proteins, spherical viruses, and bacteriophage baseplates (Fig.III.97), have been studied by several image processing methods. These include 2D rotational photographic-superposition and 2D digital rotational filtering, and 3D reconstruction. In this section, only the 2D averaging methods are discussed. Digital, rotational filtering and photographic superposition techniques produce *qualitatively* similar results, but the underlined_photographic methods should be used with caution and usually with specimens displaying obvious or well-established symmetry. Crowther and Amos (1971) and Misell (1978) compare the real-space and Fourier-space methods.
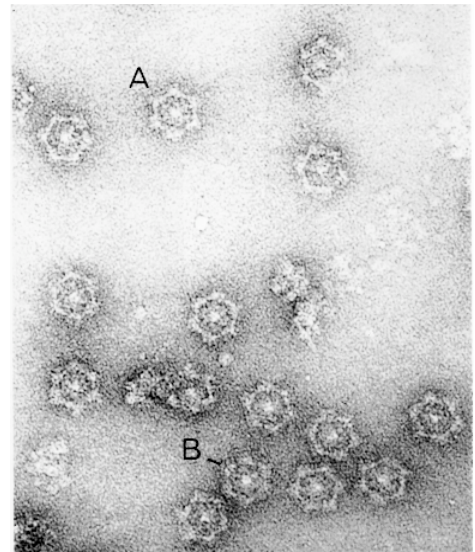
Fig.III.97 A negatively stained preparation of base plates from bacteriophage T4. Rotationally filtered images of particles A and B are shown in Fig.III.102. (From Crowther and Amos, 1971, Plate I)

1) Rotational photographic superposition method

Markham *et al.* (1963) devised a simple, real-space method for analyzing images of particles with rotational symmetry. The basic apparatus used consists of a photographic enlarger and a movable board to which a card is attached that can be rotated about an axis (Fig.III.98). The specimen image is projected onto a photographic print attached to the card and a series of *n* images are exposed onto the print, with the print rotated by *360°/n* after each of *n* exposures. For example, if the object of interest had 6-fold rotational symmetry, and a normal, straight photographic print required a 12 second exposure, then a total of six, two-second exposures would be required to produce the rotational superposition photographic image. Presumably, *maximum* reinforcement of detail is given when *n* is the true periodicity in the image of the object. This presumes, of course, that the rotation axis of the print can be positioned accurately at the center of symmetry in the image. If they do *not* coincide, the true symmetry of the object may be missed and details will certainly get smeared out in the reconstruction. Thus, the correct centering of the photographic print with respect to the rotational symmetry axis in the image and the correct choice of *n* are important components in successful application of this method. A mistake in either choice leads to erroneous results.

The main underlined_disadvantage of the optical superposition method is that it requires a visual assessment step, which may be
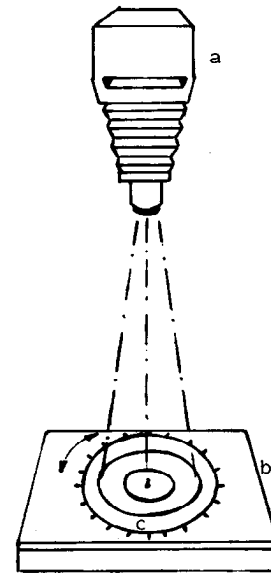
Fig.III.98. Apparatus for integrating detail in micrographs with radial symmetry. (a) Enlarger unit containing micrograph with region to be studied accurately centered in relation to the lens. (b) Movable board containing rotary disc. (c) The center of rotation must be carefully aligned to the selected region of the micrograph shown at (a). (From Horne and Markham, p.413)

more influenced, by what is eye-catching rather than what is correct. The computational, rotational filtering method that is described in the next section provides quantitative information in the form of the rotational power spectrum (RPS). The RPS allows quantitative assessment of the presence of a particular rotational symmetry. Once the symmetry is known, a filtered image can be resynthesized from only those components that obey the chosen rotational symmetry.

A second type of apparatus for producing rotationally symmetrized images by the photographic superposition method is shown below (Fig.III.99).
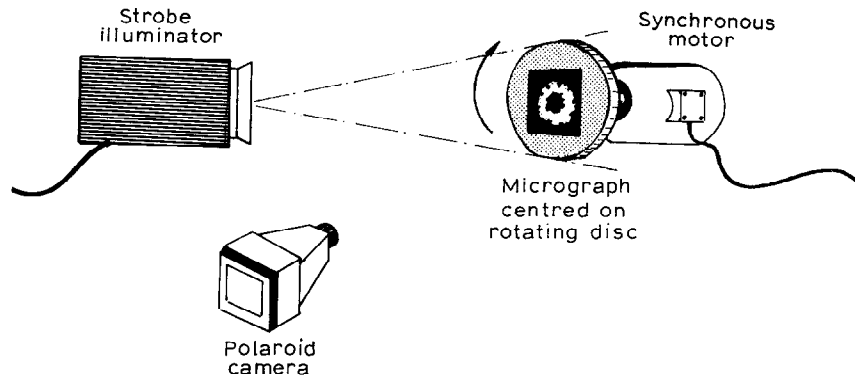
Fig.III.99. The arrangement of an apparatus for analyzing electron micrographs by rotational integration with the aid of a strobe illuminator. (From Horne and Markham, p.415)

2) 2D digital processing of rotationally symmetric particles- Power spectrum and rotational filtering analysis

Conversion from Cartesian to Polar Form

The digitization, boxing, and floating of the specimen image is performed as usual and subsequent computations are conveniently performed in polar coordinates (r,ϕ) (Fig.III.100).   Thus, a Cartesian image, $\rho(x,y)$, is converted to a polar image, $\rho(r,\phi)$, by subdividing the Cartesian image into a series of equally spaced annuli (Fig.III.101) and interpolating the densities within each annulus.   The polar density function can be expanded into a series of circular waves much as a Cartesian image is conveniently expanded into a series of plane waves (Fig.III.101).
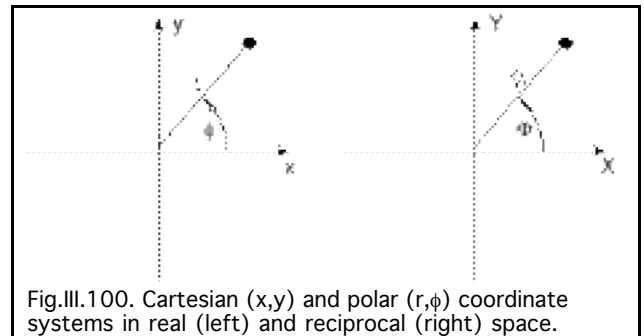

Fig.III.100. Cartesian (x,y) and polar (r,ϕ) coordinate systems in real (left) and reciprocal (right) space.
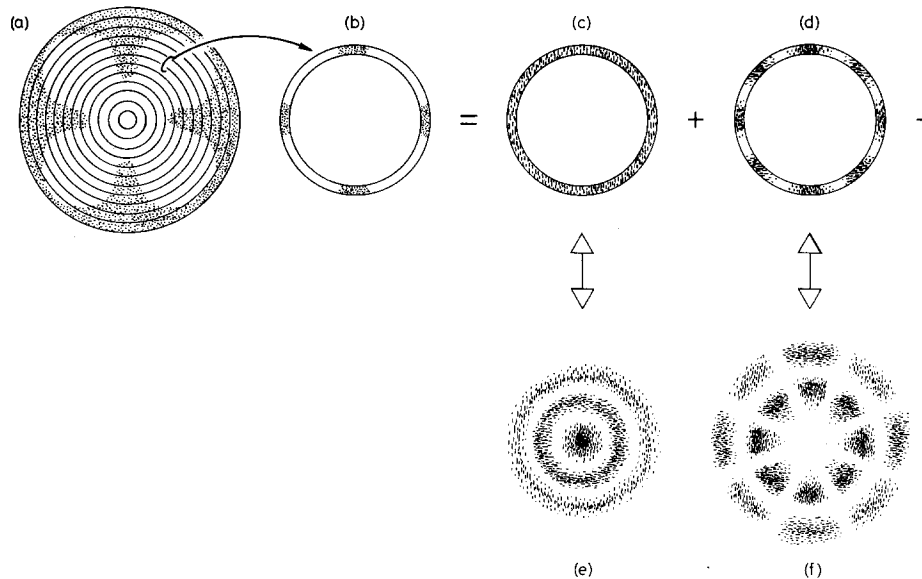

Fig.III.101. The Fourier method for finding rotational symmetry. The image (a) is divided into a series of concentric, equal-spaced annuli, of which one (b) is expressed as the sum of two of its rotational Fourier components ((c), the zero-fold and (d) the eight-fold symmetric component). The Fourier transforms of (c) and (d) are shown in (e) and (f), respectively. (From Moody, p.239)

$$\rho(r,\phi) = \sum_{n=-\infty}^{\infty} g_n(r)e^{in\phi} \qquad (1)$$

In equation (1), each $g_n(r)$ represents the weight of the n-fold azimuthal component of the image at a radius r. The phase term, $\exp(in\phi)$, positions the peak of each circular wave with respect to an origin (usually the x axis) so that all $g_n(r)$ are properly summed.

Rotational Power Spectrum

Each $g_n(r)$ is integrated over the radius of the particle, a, to obtain a measure of the total n-fold rotational component of the image. Power in the image is defined as:

$$P_n = \varepsilon_n \int_0^a |g_n(r)|^2 2\pi r dr, \qquad\qquad \varepsilon_n = \begin{cases} 1 \; for \; n = 0 \\ 2 \; for \; n > 0 \end{cases} \qquad (2)$$

ε_n = 2 accounts for the fact that P_n has equal contributions from g_n and g_{-n} for n>0.

The rotational power spectrum is a plot of P_n as a function of n. This is a compact way to represent the rotational symmetry components in the image. P_0 is usually normalized to 1.0 and the spectrum is displayed with the P_n on a logarithmic scale (Figs.III.102 and 103).
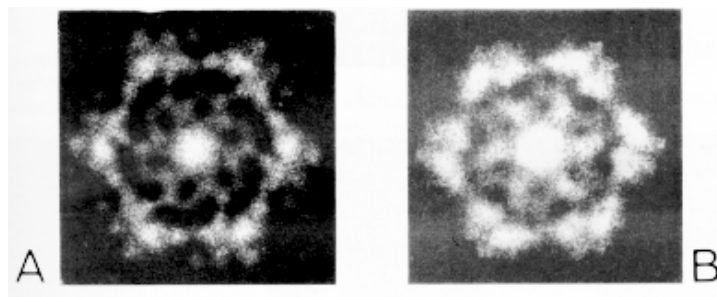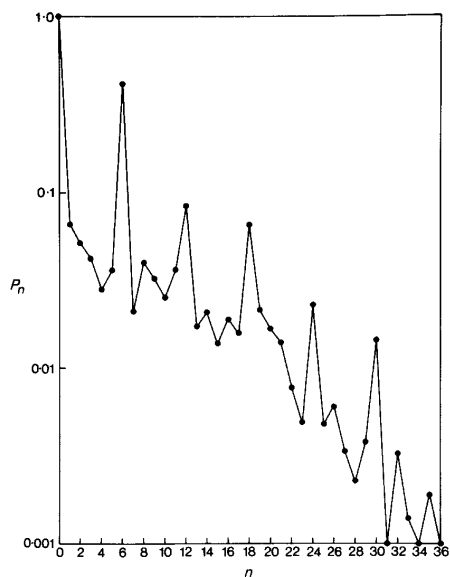

Fig.III.102. (Left) A logarithmic plot of the rotational power spectrum of a T4 bacteriophage base plate (particle A in Fig.III.97), showing the strong 6-fold symmetry of the image. The curve is normalized with P_O = 1 and the power associated with rotational frequencies higher than n = 36 is less than 0.001. (From Crowther and Amos, 1971, Fig.2, p.126). (Top) 6-fold rotationally-symmetrized images of negatively stained base plates from bacteriophage T4 (particles labeled A and B in Fig.III.97). Although the two filtered images have rather different appearances, because they have been plotted at different density levels, the main features of each are very similar. (From Crowther and Amos, 1971, Plate I)
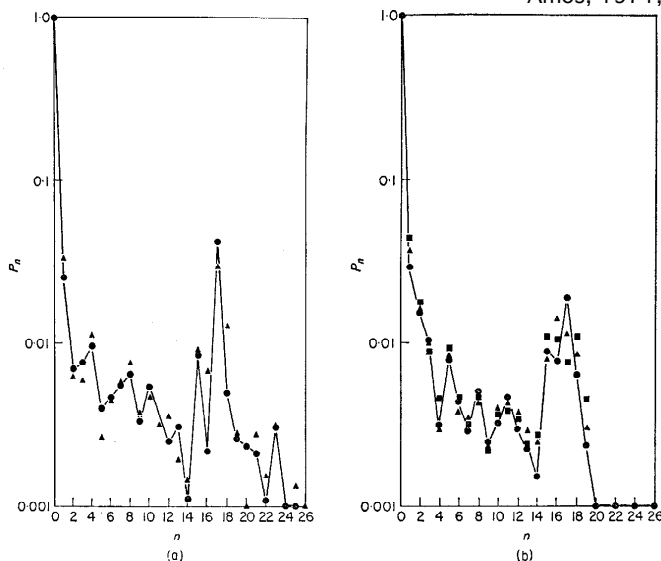

Fig.III.103. Logarithmic plots of the rotational power spectra of two images of discs of tobacco mosaic virus protein. (a) A well-preserved disc (Fig.III.104(a)) in which no one component is dominant. In each case the solid curve (-●-) refers to a choice of origin that maximizes the 17-fold component. In (a) the triangles (▲) refer to a choice of origin which simultaneously maximizes the 16- and 18-fold components, while in (b) the triangles (▲) and squares (■) refer to choices of origin which maximize respectively the 16- and 18-fold components. The curves are normalized with P_O = 1 and the power associated with rotational frequencies higher than n = 26 is less than 0.001. (From Crowther and Amos, 1971, p.127)
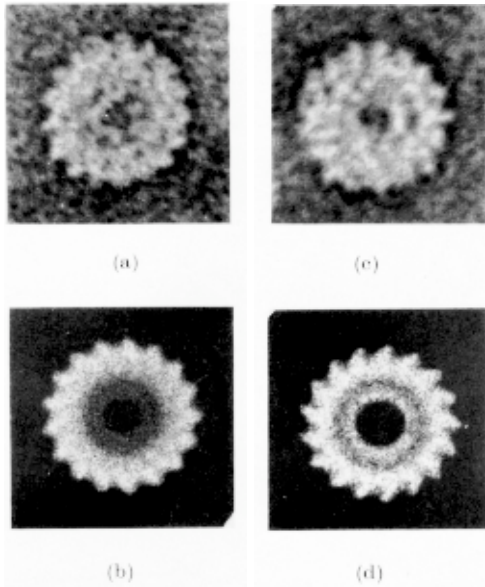
Fig.III.104. (a) and (c) Images of negatively stained discs of tobacco mosaic virus protein. (b) and (d) Results of 17-fold filtering of the images shown in (a) and (c), respectively. These images are well preserved as judged by the dominance of a single rotational symmetry in the power spectrum (Fig.III.103(a)). Note that the two filtered images, which have been processed in an identical manner, are of opposite hand, thus confirming the polar nature of the disc. The density level in plotting has been chosen to be rather high in order to emphasize the azimuthally varying component, thereby accentuating the hole at center of the particle. (From Crowther and Amos, 1971, Plate II)
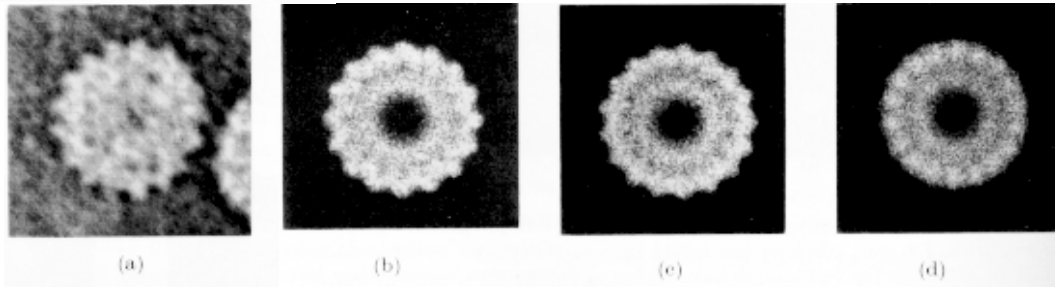

Fig.III.105. (a) Image of a negatively stained disc of tobacco mosaic virus protein. This is a poorly preserved particle as judged by the rotational power spectrum (Fig.III.103(b)). (b), (c), and (d) show respectively the results of 16-, 17- and 18-fold filtering. 16-fold filtering produces the most eye-catching image, although it is not the strongest harmonic. (From Crowther and Amos, 1971, Plate III)

3) Fourier Bessel Transform

As with other types of specimens, it is convenient with rotationally-symmetric specimens to perform computations in Fourier space rather than real space. The polar Fourier transform coordinates are R and Φ. The transform is expanded in the following way:

$$F(R,\Phi) = \sum_{n=-\infty}^{n=+\infty} \int_0^a g_n(r)J_n(2\pi rR)e^{in(\Phi+\pi/2)}2\pi r dr \qquad (3)$$

$$= \sum_{n=-\infty}^{n=+\infty} G_n(R)e^{in(\Phi+\pi/2)} \qquad (4)$$

$J_n(X)$ is a Bessel function of order n. Each J_n is a circularly-symmetric, oscillatory function (Fig.III.106). The first maximum of $J_n(X)$ for large n (i.e. $n >$ about 5) appears at about $X = n+2$.

The transform of a ring of radius a is given by $2\pi aJ_0(2\pi aR)$ (Fig.III.107). Such a ring can be considered to be generated from a pair of points, separated by the distance $2a$ that are rotated through the angle π. A single pair of points at opposite sides of a circle gives rise to cosine fringes. When rotationally averaged, the fringes reinforce at the origin but tend to cancel away from the origin. This gives rise to a Bessel function of zero order (J_0).
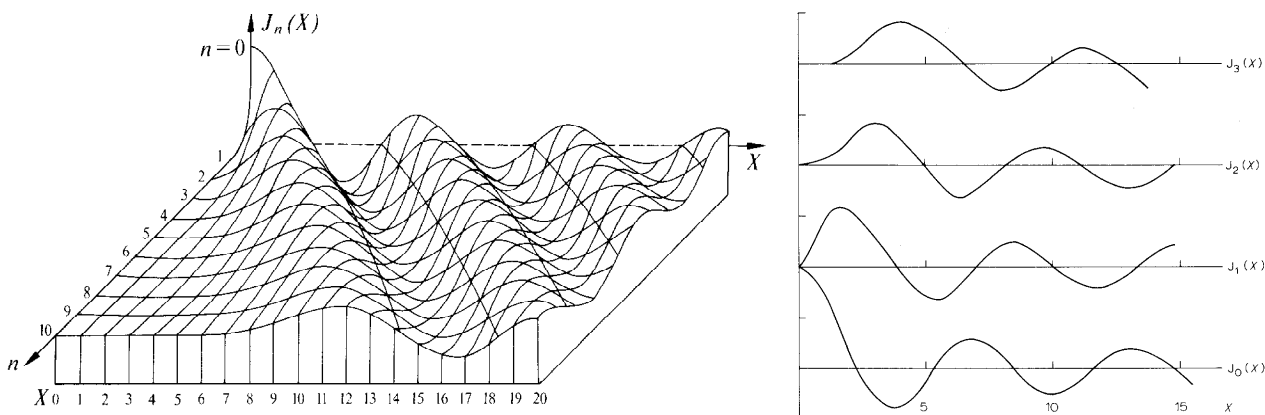
Fig.III.106. (Left) The behavior of the Bessel function $J_n(X)$ for various values of n. (From Sherwood, p. 565). (Right) Amplitude variations of the Bessel function $J_n(X)$ for $n = 0$ to 3. (From Misell, p.98)

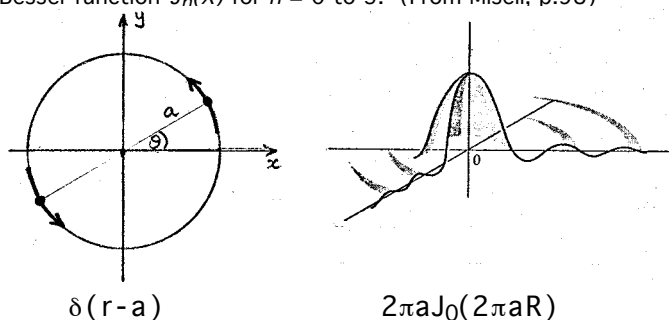$$\delta(r-a) \qquad\qquad 2\pi a J_0(2\pi aR)$$

Fig.III.107. A ring (left) and its transform (right). (Taken from Crowther unpublished course notes, 1973)

The expansion of the Fourier Transform (equation 4) is analogous to the expansion of the polar image densities as given in equation (1). Thus, the $G_n(R)$ are the coefficients (weights) of each azimuthal component in the Fourier transform. The two sets of coefficients, $G_n(R)$ and $g_n(r)$, are connected by what is called the Fourier-Bessel transform.

$$g_n(r) = \int_0^\infty G_n(R) J_n(2\pi Rr) 2\pi R dR \qquad\qquad (5)$$

In practice, the above integral would normally only be evaluated out to some resolution limit (*i.e.* with R < ∞).

The inverse relationship also holds:

$$G_n(R) = \int_0^a g_n(r) J_n(2\pi rR) 2\pi r dr \qquad\qquad (6)$$

where r_0 is the radial limit of the object.

Examples of the relationship between objects with n-fold sinusoidal variations in azimuth ($g_n(r)$) and the corresponding Fourier-Bessel transforms ($G_n(R)$) are illustrated in Fig.III.108.

4) Phase Origin

It is **essential** that the origin of the polar coordinate system lie **on** the symmetry axis of the image. Initially, the origin chosen by eye during the boxing procedure necessarily becomes the phase origin of the Fourier transform. The origin point is then shifted to get the best P_n for the assumed symmetry. By changing the assumed symmetry, m, one gets a series of origins and computes for each of these separate origins a series of rotational power spectra. These are compared to look for the dominant symmetry.

$\delta(r-r_0)\cos 2\varphi$

$-J_2(2\pi r_0 R)\cos 2\Phi$

$\delta(r-r_0)\cos 2\varphi$

$-J_2(2\pi r_0 R)\cos 2\Phi$

$\delta(r-r_0)\cos 3\varphi$

$-iJ_3(2\pi r_0 R)\cos 3\Phi$

$\delta(r-2r_0)\sin 2\varphi$

$-J_2(2\pi 2r_0 R)\sin 2\Phi$

$\delta(r-r_0)\cos 4\varphi$

$J_4(2\pi r_0 R)\cos 4\Phi$

$\delta(r-3r_0)\cos 2\varphi$

$g_2(r)$

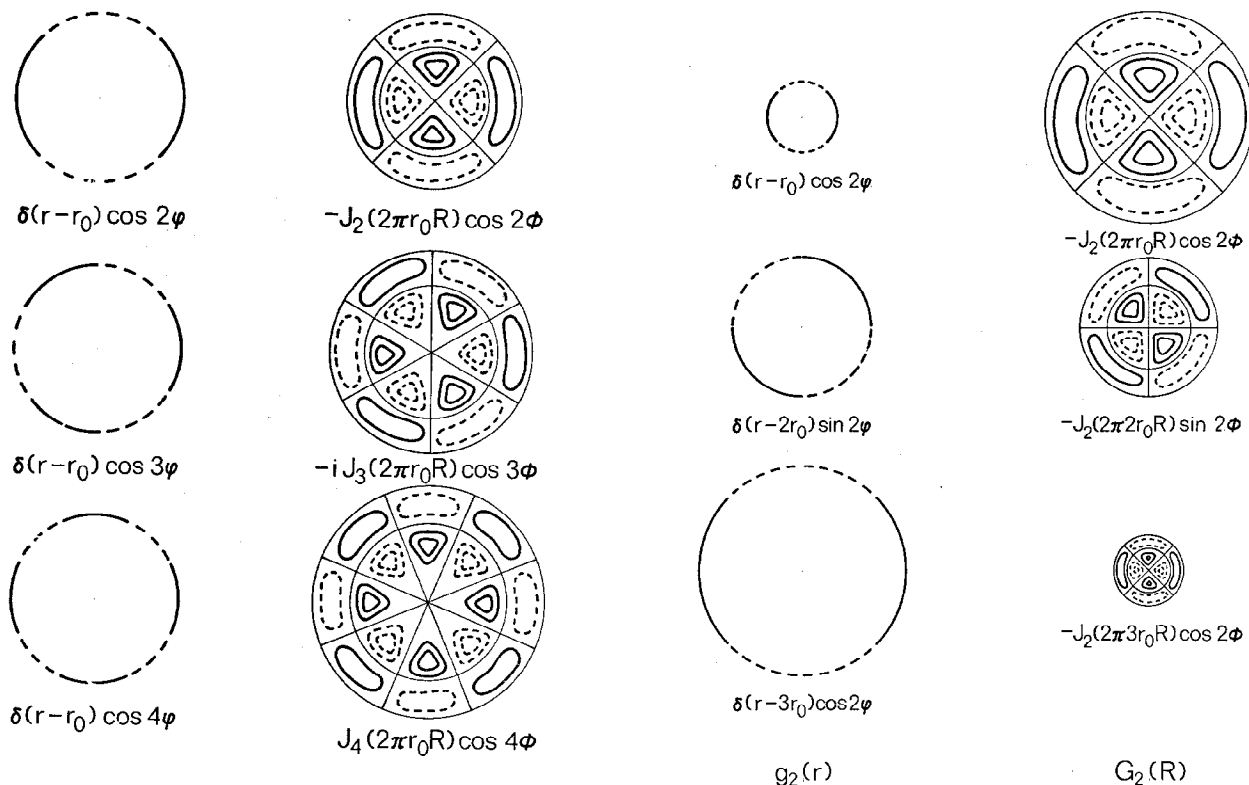$-J_2(2\pi 3r_0 R)\cos 2\Phi$

$G_2(R)$

Fig.III.108. (Left two columns) Density functions with 2-, 3-, and 4-fold azimuthal variations and the corresponding Fourier-Bessel transforms. (Right two columns) Two-fold azimuthal density functions of different radii and orientation and the respective Fourier-Bessel transforms. (Taken from Crowther unpublished course notes, 1973)
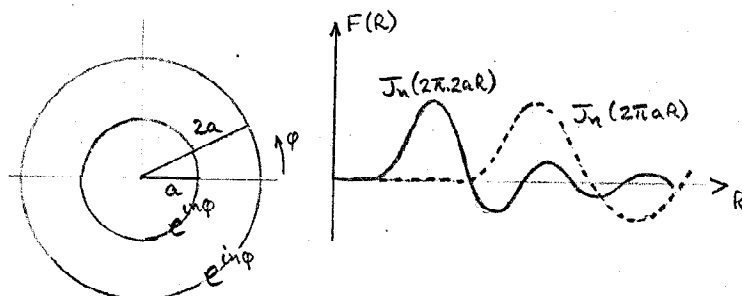
Fig.III.109. An object consisting of two rings of radii a and $2a$, each with an n-fold azimuthal variation (left) gives rise to overlapping Bessel functions which tend to cancel apart from their major peaks (right). (Taken from Crowther unpublished course notes, 1973)
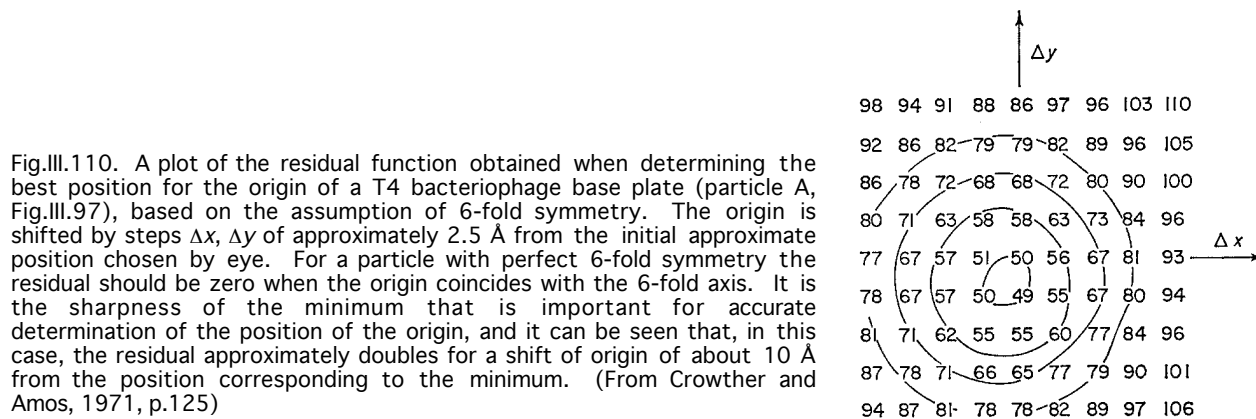
Fig.III.110. A plot of the residual function obtained when determining the best position for the origin of a T4 bacteriophage base plate (particle A, Fig.III.97), based on the assumption of 6-fold symmetry. The origin is shifted by steps Δx, Δy of approximately 2.5 Å from the initial approximate position chosen by eye. For a particle with perfect 6-fold symmetry the residual should be zero when the origin coincides with the 6-fold axis. It is the sharpness of the minimum that is important for accurate determination of the position of the origin, and it can be seen that, in this case, the residual approximately doubles for a shift of origin of about 10 Å from the position corresponding to the minimum. (From Crowther and Amos, 1971, p.125)

98	94	91	88	86	97	96	103	110
92	86	82	79	79	82	89	96	105
86	78	72	68	68	72	80	90	100
80	71	63	58	58	63	73	84	96
77	67	57	51	50	56	67	81	93
78	67	57	50	49	55	67	80	94
81	71	62	55	55	60	77	84	96
87	78	71	66	65	77	79	90	101
94	87	81	78	78	82	89	97	106

   5) Synthesis of filtered image

One typically examines the rotational power spectra computed from several different particle images to get an idea of the relative preservation of the particles. Those images that show the highest P_n are used to synthesize rotationally-filtered images. Equation (5) is used to convert each G_n to a corresponding g_n and only those g_n for which n is a multiple of m are computed, thereby omitting all other components considered to be noise. Noise may arise from several sources such as:

   1) the particle may not be viewed **directly** along an axis of symmetry

   2) the particle may be distorted or may be non-uniformly stained, shadowed, etc.

   3) the other usual forms of noise (*e.g.* support film, electron optical effects, etc.) may be present.

The $G_n(R)$ are computed from the Fourier transform by the inverse of equation (4):

$$G_n(R) = \tfrac{1}{2\pi} \int_0^{2\pi} F(R,\Phi) e^{-in(\Phi + \pi/2)} d\Phi \qquad (7)$$

In using equation (5) to compute the $g_n(r)$, n is set to some limit since P_n is effectively zero beyond certain n (resolution limit) Setting an upper limit for n, thus limits the fineness of detail that can be seen in the reconstructed image.

Note that the computation of $G_n(R)$ from $F(R,\Phi)$ (equation 7) allows the P_n to be computed either from densities directly (equation 2) or from the Fourier transform as follows:

$$P_n = \varepsilon_n \int_0^{R_{max}} \left| G_n(R) \right|^2 2\pi R dR \qquad (8)$$

Once the $g_n(r)$ are computed, equation (1) is used to resynthesize the density function, $\rho(r,\phi)$. This polar image is then reconverted back to a Cartesian format, $\rho(x,y)$, and displayed (*e.g.* Figs. III.102, 104, and 105).

   5) Comparison of Numerical and Photographic Superposition Methods

Recall the analogy of optical filtering and translational photographic superposition with crystalline (translationally symmetric) specimens (Sec.III.D.2.g, p.231). The optical diffraction pattern of such a specimen is basically a translational power spectrum of the specimen image. This diffraction pattern makes possible the objective analysis of the periodicities and preservation of the object's translational symmetry.

It is <u>not</u> possible to perform optical filtering of rotationally symmetric objects because the wanted and unwanted Fourier components are not spatially separated in the diffraction plane. Thus, it is necessary to compute the power spectrum and filter the image numerically. This procedure, like with translationally-symmetric specimens, involves two steps:

   1. Analysis (Fourier analysis) to separate the image into Fourier components.

   2. Synthesis (Fourier synthesis) to recombine just those components that satisfy the symmetry.

Photographic superposition methods attempt to determine the symmetry **AND** produce an average **at the same time**. The digital filtering approach is more reliable and powerful because of the separation of these two steps. An additional benefit of the digital processing procedure is that it provides quantitative assessment. Other advantages are that more complex operations can be performed on numerical data (*e.g.* CTF corrections), and it is a relatively straightforward procedure to combine data from a number of different images and compute difference images.